

## ORIGINAL ARTICLE

# Superior LSPR substrates based on electromagnetic decoupling for on-a-chip high-throughput label-free biosensing

Srdjan S Acimović<sup>1</sup>, Hana Šípová<sup>1</sup>, Gustav Emilsson<sup>2</sup>, Andreas B Dahlin<sup>2</sup>, Tomasz J Antosiewicz<sup>1,3</sup> and Mikael Käll<sup>1</sup>

Localized surface plasmon resonance (LSPR) biosensing based on supported metal nanoparticles offers unparalleled possibilities for high-end miniaturization, multiplexing and high-throughput label-free molecular interaction analysis in real time when integrated within an opto-fluidic environment. However, such LSPR-sensing devices typically contain extremely large regions of dielectric materials that are open to molecular adsorption, which must be carefully blocked to avoid compromising the device readings. To address this issue, we made the support essentially invisible to the LSPR by carefully removing the dielectric material overlapping with the localized plasmonic fields through optimized wet-etching. The resulting LSPR substrate, which consists of gold nanodisks centered on narrow SiO<sub>2</sub> pillars, exhibits markedly reduced vulnerability to nonspecific substrate adsorption, thus allowing, in an ideal case, the implementation of thicker and more efficient passivation layers. We demonstrate that this approach is effective and fully compatible with state-of-the-art multiplexed real-time biosensing technology and thus represents the ideal substrate design for high-throughput label-free biosensing systems with minimal sample consumption.

*Light: Science & Applications* (2017) 6, e17042; doi:10.1038/lsa.2017.42; published online 25 August 2017

**Keywords:** biosensing; hyperspectral; lab-on-a-chip; LSPR; nonspecific adsorption

## INTRODUCTION

Surface plasmon resonance (SPR) biosensing, established in the late 1980s<sup>1</sup>, is the gold standard of optical label-free sensing technologies and the most successful application of plasmonics to date<sup>2</sup>. However, during the early 2000s<sup>3</sup>, the concept of localized SPR (LSPR) sensing emerged as a convenient alternative to SPR. As the name suggests, the LSPR-sensing transduction mechanism relies on localized plasmon modes, typically excited in inert gold nanoparticles (GNPs)<sup>4–9</sup>, rather than on surface plasmon polaritons propagating on a continuous metal film. In both cases, the sensitivity is due to the delicate variation in plasmon properties with the refractive index (RI) of the dielectric material just above the metal surface. Recent studies have shown that the sensitivity of SPR and LSPR to thin molecular coatings are very similar<sup>10</sup>, but the LSPR concept presents clear advantages in terms of the simplicity of supporting optics and possibilities for high-end miniaturization, which can, for example, be utilized to enable the simultaneous interrogation of a large number of independent sensor elements on the same 'chip'. Although individual GNPs can be operated as autonomous sensors<sup>11,12</sup>, the optimal LSPR-sensing spot for most applications is considerably larger, typically containing at least a few thousand GNPs<sup>13,14</sup> to ensure a sufficiently high dynamic range and signal-to-noise ratio, and efficient molecule delivery. By combining properly designed LSPR substrates with a microfluidics

interface based on polydimethylsiloxane (PDMS) technology, the plasmonic-sensing spots can be addressed independently, and the reagent and sample consumption can be greatly reduced compared to, for example, standard enzyme-linked immunosorbent assays. The integration of micro-mechanical valves<sup>15</sup> can expand the functionality further to true lab-on-a-chip format, enabling programmable and autonomous operation<sup>16</sup>.

The existence of a well-established orthogonal surface chemistry for gold/glass surfaces based on the gold-thiol (–SH) bond gives plasmon-based optical sensors an important advantage compared to all-dielectric sensors, such as wave-guides or microresonators. However, as schematically illustrated in Figure 1a, large areas of dielectric material, the base substrate and the channel walls, are also present in an LSPR-sensing structure. This material causes nonspecific molecular adsorption, which can in turn cause unpredictable depletion of the capture and target molecules as well as a false nonspecific sensor signal due to the overlap between the plasmon-induced evanescent electromagnetic (EM) fields and the dielectric support. The issue of nonspecific adsorption in microfluidics is typically countered by introducing a passivation coating, for example, poly(1-lysine)-graft-poly(ethylene glycol)<sup>17,18</sup> or a similar non-fouling agent<sup>19,20</sup>. In the ideal case, this coating confines the biorecognition reactions exclusively to the plasmonic-sensing structures, as indicated in Figure 1b.

<sup>1</sup>Department of Physics, Chalmers University of Technology, 412 96 Göteborg, Sweden; <sup>2</sup>Department of Chemistry and Chemical Engineering, Chalmers University of Technology, 412 96 Göteborg, Sweden and <sup>3</sup>Centre of New Technologies, University of Warsaw, Banacha 2c, 02-097 Warsaw, Poland

Correspondence: SS Acimović, E-mail: srdjan.acimovic@chalmers.se; M Käll, E-mail: mikael.kall@chalmers.se

Received 22 November 2016; revised 2 March 2017; accepted 8 March 2017; accepted article preview online 10 March 2017

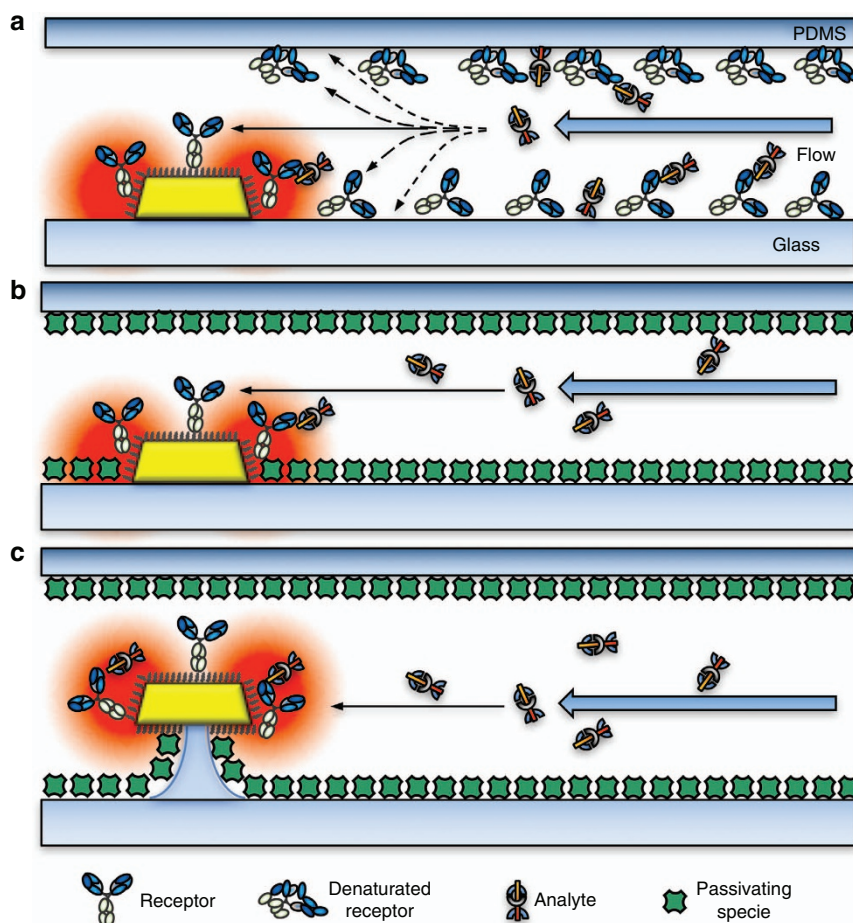


**Figure 1** Nanoplasmmonic molecular sensing in microfluidic channels. (a) Nonspecific binding will deplete both the receptor and the target molecular concentrations if the channel has not been passivated, leading to delayed sensor response, and high receptor and target consumption. Arrows represent possible interaction paths of analyte molecules. (b) Passivation of the channel surfaces with suitable blocking species reduces nonspecific binding, but the blocking molecules occupy a large portion of the most sensitive plasmonic detection volume. (c) By elevating the metal particle on an optimized nanopillar, the plasmonic fields decouple from the substrate and the passivation molecules. This configuration significantly increases the effective sensing volume and improves the overall sensor performance.

Unfortunately, the majority of reported passivation strategies<sup>17–23</sup> are challenging to apply to structures that contain several different kinds of interfaces, such as PDMS, SiO<sub>2</sub> and gold, due to factors including cross-contamination, differences in hydrophobicity/hydrophilicity<sup>24</sup>, solvent incompatibility<sup>25</sup>, device assembly issues and so on. Moreover, even if the dielectric support surrounding the plasmonic-sensing structure is successfully passivated without interfering with the sensor functionalization, which is extremely challenging, it would still occupy a large proportion of the plasmonic near-field (Figure 1b), resulting in reduced sensitivity. Here we address these issues by instead engineering plasmonic substrates to be intrinsically immune to the signals caused by nonspecific substrate adsorption. This goal can be achieved by positioning disk-shaped GNPs on narrow pillars optimized so that the plasmonic probing volume falls completely outside and is decoupled from the dielectric support material, as indicated in Figure 1c. The idea of elevating gold nanodisks above the substrate to increase the LSPR sensitivity to RI changes was introduced by Dmitriev *et al.*<sup>26,27</sup> and later followed up by several research groups<sup>28–30</sup>. In particular, Sepulveda and co-workers<sup>29</sup> demonstrated that wet-etching could be used to achieve a significant undercut beneath the Au nanodisk, resulting in pillar-like structures with ca.

50% enhanced sensing performance for small target DNAs. However, to the best of our knowledge, none of these studies demonstrated complete EM decoupling or made the connection to the issue of nonspecific adsorption in the context of LSPR high-throughput sensing. Here we optimize the technique pioneered by Otte *et al.*<sup>29</sup> to maximize the EM decoupling effect without compromising the mechanical integrity of the nanodisk sensors. We then demonstrate that samples fabricated in this way exhibit markedly reduced sensitivity to nonspecific substrate adsorption, which is later exploited as a passivation step in our model system biosensing protocol. Furthermore, we show that it is possible to micropattern the samples inexpensively using PDMS stamps and to interface such plasmonic substrates with advanced microfluidics architectures.

## MATERIALS AND METHODS

### Fabrication of sensing substrates

Glass slides (24 × 24 mm #5) were cleaned by 5 min sonication in acetone and isopropanol, and then covered by sputter deposited titanium (1 nm) and gold (50 nm), as indicated in Figure 2a. The substrates were then briefly treated in oxygen plasma prior to the drop casting of positively charged PDDA (poly-diallyldimethylammonium

chloride, 0.2 volume % in water, Sigma-Aldrich), as shown in Figure 2b. After a short water rinse, a solution of negatively charged polystyrene (PS) beads (0.1% in water, Microparticles GmbH, Germany) was drop casted on the substrates (Figure 2c). Depending on the application, either the PS beads were removed from half of the substrate surface with dicing tape, or the substrates were patterned by PDMS micro-contact printing (Figure 2d). The self-assembled PS beads acted as a mask during subsequent ion-beam milling (Ionfab 300, Oxford Instruments, UK; Figure 2e). The PS beads were then removed by dicing tape, and the substrates were treated in oxygen plasma to remove the remaining PDDA fragments (Figure 2f).

#### Fabrication of PDMS structures

The mold for micro-contact printing was made by laser-writing lithography on a silicon wafer (mrDWL 5-negative photoresist, Allresist GmbH, Germany). The process parameters were tuned according to the manufacturer's recommendations. A bubble-free PDMS mixture (10:1, Sylgard 184 kit, Dow Corning, USA) was spin-coated on the mold at 250 r.p.m. After being kept in the dark for ~40 h, this process resulted in a final PDMS thickness of 0.75–1 mm. The sticky PDMS membrane was carefully peeled off, rolled over the PS-covered gold substrate, where it was kept in contact for 10–20 s, and then removed in one smooth move. Detailed descriptions of the PDMS microfluidic fabrication procedure can be found elsewhere<sup>31,32</sup>.

#### Optical spectroscopy

Ensemble averaged extinction spectra were recorded on a UV-VIS-NIR spectrophotometer (Cary 2000, Agilent Technologies, USA). Real-time tracking of the LSPR wavelength of single sensing spots was performed using a home-built extinction set-up based on a collimated fiber-coupled light source (HL-2000, Ocean Optics, Dunedin, USA) and a fiber-coupled spectrometer (BRC711E, B&W Tek, USA). Simultaneous measurements of multiple sensing spots were performed using a hyperspectral imaging set-up<sup>33,34</sup> built around an inverted microscope (Eclipse Ti-E, Nikon, Japan), a liquid crystal tunable filter (LCTF, 650–1100 nm spectral range, 7 nm bandwidth, 1 nm resolution, model Varispec SNIR, PerkinElmer, USA) and a CMOS camera (Neo5, Andor Technologies, UK). Our system has been specially designed for the real-time parallel interrogation and on-the-fly analysis of multiple sensing sites by synchronizing and controlling all essential optical components using custom-made Labview code.

#### Electrodynamics simulations

Simulations of optical spectra and near-field distributions were conducted using a commercial finite-difference time-domain (FDTD) implementation (Lumerical, Inc., Canada) with optical constants for gold based on<sup>35</sup> and a total-field/scattered-field formulation. The simulated gold disks had diameters  $d=172, 200$  or  $280$  nm, thickness  $t=60$  nm, a curvature of the top and bottom edges of radius 5 nm, and a side taper angle of  $20^\circ$ . The RI of the substrate/pillar support was set to  $n=1.52$ , and the structures were surrounded by water ( $n=1.33$ ). The mesh size was 4 nm but refined to 0.5 nm around the disks and the etched profiles.

#### Surface chemistry

First, 0.1 mM SH-PEG-methoxy (5 kDa, Rapp Polymere, Germany) was dissolved in ethanol at  $50^\circ\text{C}$ . The substrates were immersed in PEG solution overnight and then attached to the PDMS microfluidic structures by low-temperature thermal bonding ( $40^\circ\text{C}$ ) for 2–3 h. Anti-PEG immunoglobulin Gs (IgGs) E11 and E6.3 were received in 50% glycerol at a concentration of  $400\ \mu\text{g ml}^{-1}$  (Ref. 36). Neutravidin

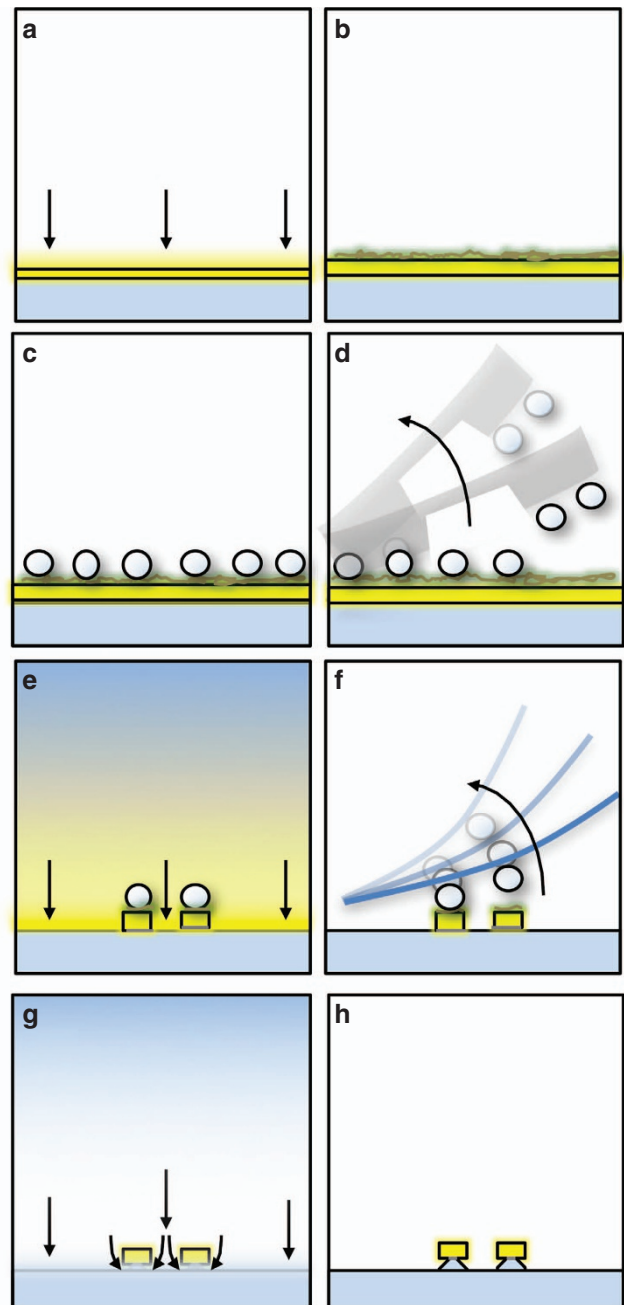


**Figure 2** Fabrication of nanopillar-supported Au nanodisks. The steps in the fabrication process are as follows: (a) material sputtering; (b) drop casting of positively charged polymer film; (c) self-assembly of negatively charged polystyrene (PS) beads; (d) optional micro-patterning using PDMS stamp; (e) ion-beam milling; (f) removal of remaining PS beads by tape-stripping; (g) etching of glass substrate in BOE; (h) final micro-pattern containing gold nanodisks on glass nanopillars.

(NTV; ThermoFischer Scientific) was dissolved in corresponding buffer(s) to a concentration of  $50\ \mu\text{g ml}^{-1}$  and used as such.

## RESULTS AND DISCUSSION

We used the well-established, cheap and scalable colloidal lithography method<sup>37</sup> to produce well-defined patterns of short-range-ordered gold nanodisks on standard glass microscope slides. The fabrication

steps involved are schematically illustrated in Figure 2a–2f, where we have also included the optional step (Figure 2d) of two-dimensional micro-patterning based on the lift-off-free method developed by Andersson *et al.*<sup>38</sup>. This fabrication protocol yields samples fully compatible with the microfluidics devices and assay protocols previously developed by Aćimović *et al.*<sup>32</sup>. The contrast between regions with and without nanoparticles achievable through this method is excellent, as illustrated in Supplementary Fig. S1.

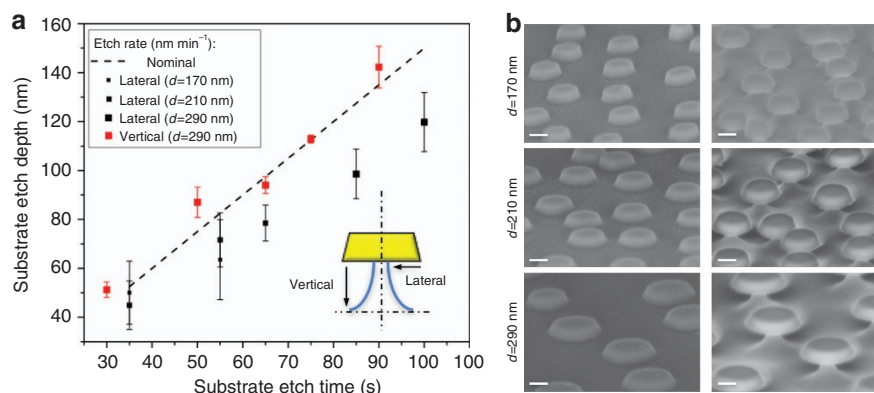
The nanodisk substrates constitute the starting point for wet-etching (Figure 2g), to generate nanodisks on narrow pillars, as introduced by Otte *et al.*<sup>29</sup>. We use a standard buffered oxide etch (BOE, 15% of hydrofluoric acid) throughout. Following a gentle water rinse to stop the etching process, the samples are dried under a stream of nitrogen. The surface tension that arises because of the retreat of the thin water layer during drying can cause the nanopillars to break, and this effect sets a limit on how thin a nanopillar can be, which, in turn, limits the minimum nanodisk diameter needed to achieve EM decoupling. For this reason, we focused on gold nanodisks with larger diameters,  $d$ , than explored previously<sup>29</sup>.

Figure 3 summarizes morphological changes versus etching time for three different Au nanodisk samples with  $d=170$ – $290$  nm. We hypothesized that the etching rates might be anisotropic due to the three-dimensionally nanostructured landscape. To test this possibility, we first determined the vertical etching rate by profilometer scans across boundaries with and without  $d=290$  nm nanodisks. As seen in Figure 3a, these data are in excellent agreement with the known nominal etch rate of glass in BOE in our lab ( $\sim 90$  nm min<sup>-1</sup>). We then imaged the substrates using a scanning electron microscope (SEM) at a tilt angle of 70° to estimate the lateral etch depth directly underneath the nanodisks, obtained as  $(d-d')/2$ , where  $d'$  is the diameter of the nanopillar closest to the nanodisk. The data in Figure 3a suggest a lateral etch rate of 77.5 nm min<sup>-1</sup> (linear fit), demonstrating a pronounced but favorable etching anisotropy, presumably due to diffusion inhomogeneity. Finally, based on the SEM image analysis, we estimated the minimum mechanically stable nanopillar diameter to be  $d'\approx 50$  nm. Figure 3b compares non-etched disks (left) and disks supported by  $d'\approx 50$  nm nanopillars (right).

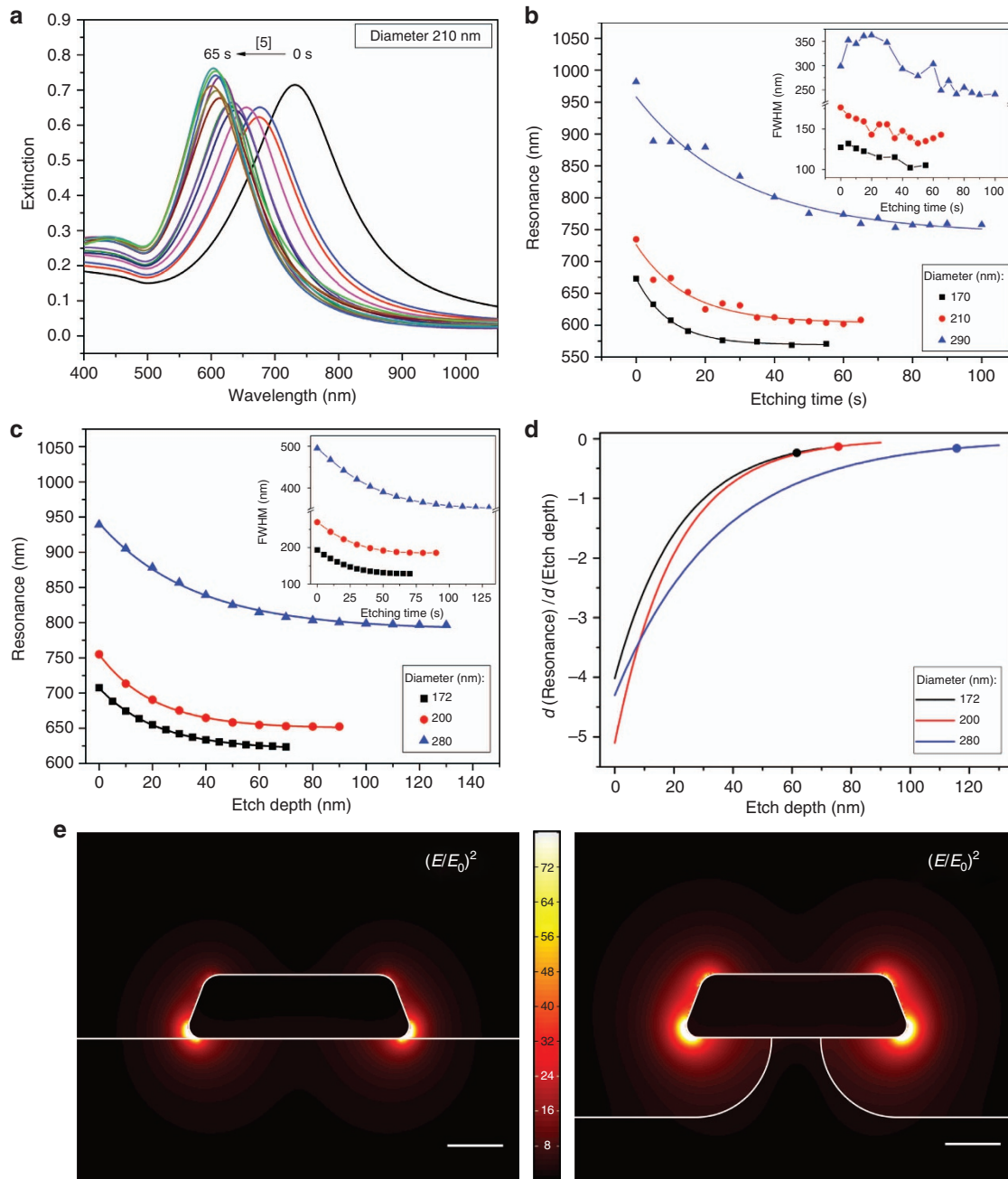
We measured optical extinction as a function of etching time to quantify the degree of EM decoupling versus pillar morphology. Figure 4a illustrates typical spectral evolution during etching for the case of 210 nm disks (for 170 and 290 nm disks, see Supplementary

Fig. S2). It is obvious that the dominant LSPR, which corresponds to a dipolar charge oscillation in the plane of the disk, undergoes a continuous blue shift and narrowing upon pillar formation. The blue shift is a result of the decreasing average RI within the plasmonic near-field. We interpret the narrowing as due to the more symmetric dielectric environment around the disks. In Figure 4b, we plot the resonance peak wavelength versus etching time for the three nanodisk diameters considered. The resonance evolution can be fitted well with an exponential decay towards a static value,  $\lambda_{\text{LSPR}}(t) - \lambda_{\text{LSPR}}(\infty) \propto \exp(-t/\tau)$ , with a time constant  $\tau$  that increases with the disk diameter ( $9.8 \pm 1.1$ ,  $14.29 \pm 5.9$  and  $24.69 \pm 10.1$  s), indicating a larger sensing volume for larger disks. More importantly, the change in resonance position versus time levels out and enters a plateau region (that is, approaching  $\lambda_{\text{LSPR}}(\infty)$ ) after a certain size-dependent etching time, indicating that we have reached the EM decoupling regime in which the dipolar plasmonic near-field no longer 'sees' the supporting nanopillar. Figure 4b shows that the EM decoupling regime begins at an etching time of ca. 40, 50 and 75 s for the 170, 210 and 290 nm nanodisk substrates, respectively. Ideally, one would like to be as far as possible at the right side of the plateau region, as long as the mechanical stability of the nanopillars is preserved. For instance, at the threshold of mechanical stability for the 210 nm disks, corresponding to a 65 s etching time, a 20 nm-thick passivation layer would still reside mainly within the 'invisible zone' according to the etching rates extracted from Figure 3a. In addition, the substantial reduction in LSPR linewidth (see the inset of Figure 4b), is highly beneficial because it results in lower baseline noise levels when tracking the LSPR position in sensing experiments<sup>39</sup>. Spectroscopic tracking can also be used to precisely identify the point when substrate over-etching induces mechanical instability of the nanopillars, which results in broad and red-shifted resonances (Supplementary Fig. S3).

We performed electrostatics calculations using the FDTD method to substantiate our claim of EM decoupling and to obtain a better understanding of the optimal structure parameters. We calculated the optical response for single nanodisks of diameter  $d=172$ , 200 and 280 nm, which closely match the experimental values, but assumed isotropic etching dynamics to reduce calculation time and modeling efforts. As summarized in Figure 4c, the calculated peak positions display a similar exponential trend to the one observed in the experiments. The LSPR linewidths also exhibit an exponential



**Figure 3** Formation of nanopillars underneath gold nanodisks by etching in BOE. (a) Vertical (red data points) and lateral (black points) etch depths of glass for substrates covered with gold nanodisks of various diameter  $d$ . The nominal etch rate of ca. 90 nm min<sup>-1</sup> is indicated by the dashed line. Error bars represent the standard deviation of the data sets. (b) SEM images at 70° tilt angle of representative populations of unmodified and etched gold nanodisks of varying diameter  $d$  (scale bar = 100 nm).



**Figure 4** Optical properties of gold nanodisks versus etching time. **(a)** Experimental extinction spectra in air as a function of substrate etching time for nanodisks with diameter  $d=210$  nm. **(b)** Plasmon resonance peak positions and linewidth (inset in full width at half maximum, FWHM) as functions of substrate etching time and disk diameter for nanodisks with  $d=170$ , 210 and 290 nm. Lines show exponential fits to data. Note that a plateau is reached after a certain etch time, signaling EM decoupling between the disks and the glass substrate. **(c)** Calculated resonance position as a function of etching depth for  $d=172$ , 200 and 280 nm disks. The inset shows the linewidth evolution as a function of etching depth. **(d)** Calculated derivative of resonance position versus etching depth. The discrete points mark the etching depth for which the nanopillar diameter has reached a diameter  $d=50$  nm, corresponding to the experimentally determined minimum value that yields undisturbed mechanical stability. **(e)** Calculated intensity enhancement maps at resonance showing spatial extension of sensing volume for a 200 nm nanodisk directly on glass (left,  $\lambda=752$  nm) and supported by a 50 nm glass nanopillar (right,  $\lambda=652.5$  nm).

decay (Figure 4c, inset), although the experiments only showed a general decrease in full width at half maximum, probably due to inhomogeneous broadening, for example, from the size polydispersity of PS beads (Figure 4b, inset). The calculations reveal that the resonance plateaus are not entirely flat, partly because of the assumed isotropic rather than anisotropic etching, but they do have very low

slopes after a certain time. We checked the derivative of the resonance position as a function of etching depth to determine the highest degree of EM decoupling attainable for the chosen minimum nanopillar diameter  $d'=50$  nm (Figure 4d). The data show that the minimal absolute value,  $\sim 0.12$  nm per nm of adsorbed layer thickness, is obtained for the 200 nm disks. The initial derivatives, at zero etch

depth, represent the response of the disks to an infinitesimally thin layer with  $RI = 1.52$  formed on the glass. For the 200 nm disk, this value is  $\sim 5.01$ , that is,  $\sim 40$  times higher than the derivative value for the same disk supported by a  $d = 50$  nm pillar. Thus, the nanodisk is essentially decoupled from the substrate for the optimally etched structure. Figure 4e illustrates the corresponding changes in EM near-field intensity at resonance for these two limiting cases, indicating a significant reduction in field–substrate spatial overlap for the pillar-supported nanodisk.

To demonstrate the advantage of EM decoupling for biosensing applications, we choose to work with a simple model system resembling the ideal assay strategy as illustrated in Figure 1b and 1c. We use NTV as a passivating entity due to its almost irreversible adsorption to glass at neutral pH<sup>40</sup>. The receptor is a 5 kDa thiol-PEG-methoxy that binds exclusively to gold and repels proteins efficiently<sup>41</sup>, thus fulfilling the requirement of low cross-contamination between the passivating species and the receptor biorecognition layer. We first investigated the LSPR response of PEG-coated nanodisks to NTV ( $50 \mu\text{g ml}^{-1}$ ), which is thus expected to bind almost exclusively to the glass substrate. Figure 5a summarizes the response upon injection of NTV of 210 nm disks subjected to 0, 10, 30 and 50 s of etching in BOE. For the longest etching time used, which is considerably shorter than the 65 s limit determined for the 210 nm disks, the response drops by approximately an order of magnitude compared to the non-etched case (see inset of Figure 5a for absolute peak-shift values).

The data in Figure 5a clearly show that nanopillar formation drastically reduces the LSPR sensitivity to NTV adsorption on the substrate. However, for this effect to be useful, we also need to show that the LSPR sensitivity to target molecules is not compromised. We achieve this verification by simultaneously comparing the response of standard and pillar-supported nanodisks fabricated on two parts of the same glass substrate. To ensure that the surface chemistry of the standard and supported nanodisks are comparable, half of the sample

was first exposed to BOE for 45 s, after which the whole sample was briefly dipped into BOE for 5 s. The whole sample was then incubated with thiol-PEG-methoxy overnight, rinsed and then interfaced to a single-channel PDMS fluidics device (see Supplementary Fig. S4b). Using our hyperspectral imaging spectroscopy measurement system, we could then simultaneously trace the LSPR response of the ‘standard’ (that is, 5 s etched) and pillar-supported (that is, 50 s etched) nanodisks in real-time. As summarized in Figure 5b, we successively exposed the sample to three different kinds of RI perturbations: (1) NTV ( $50 \mu\text{g ml}^{-1}$ ) in phosphate-buffered saline (PBS) buffer, which tests the sensitivity to nonspecific interactions with the substrate, as in Figure 5a, followed by a rinse; (2) a test of the bulk RI sensitivity by injecting PBS buffer containing 2.5% glycerol and NTV ( $50 \mu\text{g ml}^{-1}$ ); and (3) a test of the analyte sensitivity, performed by injecting a PEG-specific antibody<sup>36</sup> (E11 IgG,  $20 \mu\text{g ml}^{-1}$ ) dissolved in PBS containing 2.5% glycerol and  $50 \mu\text{g ml}^{-1}$  NTV, followed by a rinse. The data in Figure 5b again show that the sensitivity to nonspecific substrate binding is reduced for the pillar-supported nanodisks, this time by a factor of 4–5 (the theoretical reduction factor is 13, as calculated by integration of the derivative in Figure 4d over a 4.5 nm-thick NTV layer<sup>42</sup>). In agreement with earlier reports on elevated nanoplasmonic structures<sup>26,29</sup>, the pillars also increase the bulk RI sensitivity by almost a factor of two, and more importantly, they increase the analyte sensitivity by  $\sim 25\%$ . Thus, we can conclude that all essential sensing characteristics of the nanodisk LSPR sensors are improved by EM decoupling, as summarized in the inset of Figure 5b.

Although working with microfluidics channels directly interfaced with pillar-supported nanodisks, such as the one used for the measurements in Figure 5b, we found that the microfluidics devices sometimes suffered from leakage and delamination issues (see Supplementary Fig. S4b for an example). This result is not very surprising, considering that the top face of the nanodisks can be

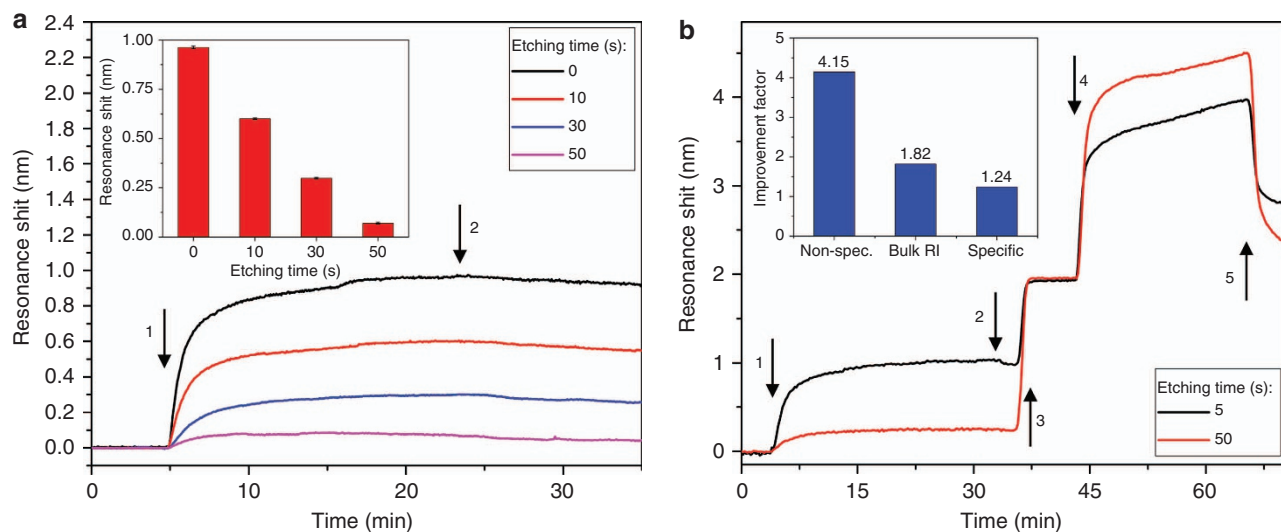


**Figure 5** EM decoupling in LSPR biosensing. **(a)** Response of PEG-coated gold nanodisks upon injection (arrow 1) of NTV ( $50 \mu\text{g ml}^{-1}$ ) versus substrate etching time in BOE. Arrow 2 denotes the buffer rinsing step. Inset shows the final resonance shift. The test device is shown in Supplementary Fig. S4a. Error bars represent the uncertainty in determination of the resonance shift. **(b)** Simultaneous response of 5 and 50 s etched gold nanodisk areas under exposure to various analyte model systems: NTV (nonspecific adsorption to glass), bulk RI change and PEG-specific IgG antibody detection. The sequence of injection steps is as follows: (1) NTV ( $50 \mu\text{g ml}^{-1}$ ) in PBS buffer, (2) PBS buffer rinse, (3) injection of 2.5% glycerol in NTV ( $50 \mu\text{g ml}^{-1}$ )-spiked PBS, (4) injection of anti-PEG E.11 antibody ( $20 \mu\text{g ml}^{-1}$ ) in 2.5% glycerol PBS buffer spiked with NTV ( $50 \mu\text{g ml}^{-1}$ ). Note the inverse ratio of the response between 5 and 50 s etched substrates for the substrate (NTV) and sensor-specific analyte (anti-PEG antibody). Inset shows improvement factor of 50 s etched structures over 5 s etched for the case of nonspecific interaction of NTV to glass, bulk RI change and specific interaction of Ab. The most dramatic change is observed for nonspecific protein adsorption on glass. The test device is shown in Supplementary Fig. S4b.

>150 nm above the bottom glass surface for optimally etched samples, which makes it difficult for the PDMS interface to deform and establish a firm bond with the substrate. Leakage is not a major issue if wide channels are used, when the liquid pressure can be kept low, but for miniaturized multiplexed sensing, the substrate needs to be patterned so that the pillar-supported nanodisks reside only inside channels. Two-dimensional patterning on the micrometer-scale can easily be achieved using PDMS stamps, as demonstrated here or by Andersson *et al.*<sup>38</sup>, but it is challenging to precisely align such complex patterns with narrow-channel microfluidics structures without compromising the functionality of the device or the total cost. We therefore decided to test whether the simplified architecture used by Chen *et al.*<sup>27</sup> and Aćimović *et al.*<sup>32</sup>, consisting of lines of plasmonic nanoparticles running perpendicular to microfluidic channels, could be applied to pillar-supported nanodisk substrates. The test device consists of 210 nm disks supported on  $d' = 50$  nm-narrow pillars patterned into eight parallel 100  $\mu\text{m}$ -wide stripes with a separation of 150  $\mu\text{m}$ . The patterned substrate was cross-aligned with an active microfluidic structure with eight parallel 100  $\mu\text{m}$ -wide channels with 100  $\mu\text{m}$  separation and hemispherical cross-section radii of 16  $\mu\text{m}$ . The final device, shown in Figure 6a, contains 64 sensing spots with a packing density of  $\sim 20 \text{ mm}^{-2}$ . During the course of standard operation, using pressure driven flows of  $< 1 \mu\text{l min}^{-1}$ , we did not observe any leakage or chip delamination in  $> 10$  tested devices. Importantly, we did not observe any cross-contamination between channels through the plasmonic stripes, where bonding is expected to be the weakest. Finally, we used this kind of device to measure the biorecognition reaction of two antibodies (E11 and E6.3 IgGs) targeting the PEG receptor. Prior to antibody injection, the channels were passivated with NTV as before. We then injected the IgGs, in concentrations within the range recommended by the supplier, at  $0.5 \mu\text{l min}^{-1}$  for 30 min and then switched to rinsing buffer ( $50 \mu\text{g ml}^{-1}$  of NTV in 2.5% glycerol in PBS). Interestingly, the two antibodies showed quite different binding kinetics, possibly due to differences in affinity and different epitopes, but the origin of this effect is beyond the scope of this article. More importantly, the binding curves show no evidence of concentration-dependent delays, even for the lowest concentrations detectable here ( $2 \mu\text{g ml}^{-1}$ ) during 30 min incubation. This finding may allow LSPR to be used not only for on-chip diagnostics<sup>27,32,43,44</sup> but also for determining binding rates in buffer matrices. We conclude that the micropatterned nanopillar-supported nanodisk substrates are extremely well suited for

high-throughput low-consumption opto-fluidics LSPR sensing due to their full compatibility with state-of-the-art microfluidics and read-out schemes and their less restrictive nature regarding the development of assay strategies for applications in diagnostics or the pharmaceutical industry.

## CONCLUSIONS

Elevated supports of various kinds have been previously explored as a route to increased sensitivity of plasmonic nanoresonators to RI perturbations<sup>26,28–30</sup>. The partial physical removal of the substrate around and beneath a metal nanoparticle increases the usable fraction of the plasmonic mode volume and pushes it away from the high index substrate towards the embedding aqueous medium, resulting in a sensing performance approaching that of a nanoparticle in solution. In this work, we have shown that this 'electromagnetic decoupling' approach can also be used to make the plasmonic-sensing structures almost insensitive to molecular adsorption at the dielectric support structure. We achieved this goal by carefully engineering a mechanically stable support pillar and selecting the optimal parameters of disk-shaped GNPs. The sensing properties of the optimized pillar-supported nanodisks were assessed in direct comparison to standard nanodisk substrates by exposing them simultaneously to three classes of possible RI perturbations (proteins interacting nonspecifically with the substrate, a bulk RI change and a specific analyte–biorecognition interaction) and found to be superior in all three aspects. However, the most important conclusion is that it is possible to almost entirely eliminate the sensitivity to perturbations occurring on the supporting substrate, in this case represented by the adsorption of the moderately large protein NTV. This possibility significantly simplifies the assay strategy and sensor preparation in essentially all types of LSPR biosensing applications, removing the restrictions on the size (molecular weight) of the passivating layers. In addition, we showed that nanopillar-supported gold nanodisk sensors can be easily patterned for convenient integration with state-of-the-art active microfluidics devices to achieve efficient and rapid read-out with a high signal-to-noise ratio using parallel real-time hyperspectral imaging, enabling flexible high-throughput operation. On the basis of these results, one can argue that LSPR biosensing is extremely well poised to become the next revolutionary tool for cost-effective label-free molecular interaction analysis with high sensitivity, high throughput, low sample consumption, robust instrumentation and superior miniaturization, and multiplexing capabilities.

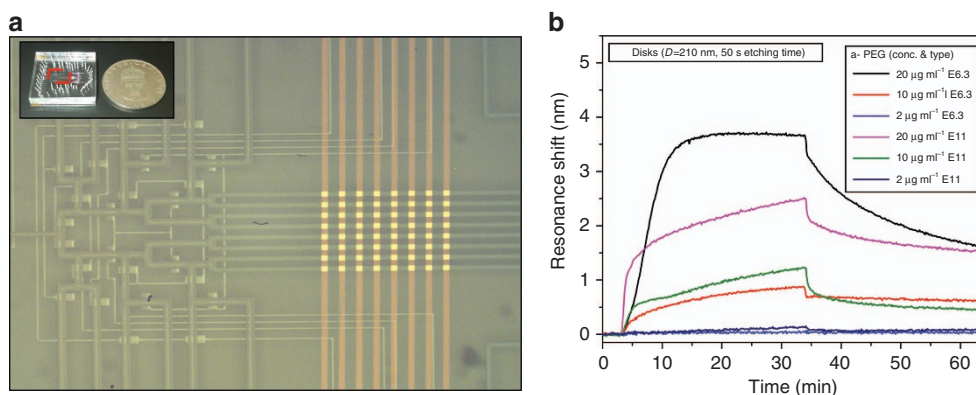


**Figure 6** Compatibility of pillar-supported disks with cross-aligning and bonding process to PDMS microfluidic large-scale-of-integration interface. (a) Portion of the device, where 64 shiny squares (at crossings between channels and micropatterned plasmonic substrate) represent 64 sensing sites. These sites were used to verify the sampling time and noise independence of the number of sensing sites (data not shown). Inset shows device ( $24 \times 24 \times 5$  mm) next to a coin (1 SEK). (b) Real-time sensogram comparing interaction of two types of anti-PEG IgGs as function of antibody concentration.

**CONFLICT OF INTEREST**

The authors declare no conflict of interest.

**ACKNOWLEDGEMENTS**

This work was supported by the Knut and Alice Wallenberg Foundation and the Swedish Foundation for Strategic Research (SSF). TJA thanks the Polish National Science Center for support via the project 2012/07/D/ST3/02152. We wish to acknowledge the Science Faculty of the University of Gothenburg for supporting the PDMS Microfluidic Fabrication Facility. SSA thanks Mark P. Kreuzer, Romain Quidant, Mikael Svedendahl and Ruggero Verre for useful discussions.

- Lundström I. From a laboratory exercise for students to a pioneering biosensing technology. *Plasmonics* 2014; **9**: 741–751.
- Homola J. Surface plasmon resonance sensors for detection of chemical and biological species. *Chem Rev* 2008; **108**: 462–493.
- Anker JN, Hall WP, Lyandres O, Shah NC, Zhao J *et al*. Biosensing with plasmonic nanosensors. *Nat Mater* 2008; **7**: 442–453.
- Aćimović SS, Kreuzer MP, González MU, Quidant R. Plasmon near-field coupling in metal dimers as a step toward single-molecule sensing. *ACS Nano* 2009; **3**: 1231–1237.
- Lukyanchuk B, Zheludev NI, Maier SA, Halas NJ, Nordlander P *et al*. The Fano resonance in plasmonic nanostructures and metamaterials. *Nat Mater* 2010; **9**: 707–715.
- Jonsson MP, Dahlin AB, Feuz L, Petronis S, Höök F. Locally functionalized short-range ordered nanoplasmonic pores for bioanalytical sensing. *Anal Chem* 2010; **82**: 2087–2094.
- Cetin AE, Altug H. Fano resonant ring/disk plasmonic nanocavities on conducting substrates for advanced biosensing. *ACS Nano* 2012; **6**: 9989–9995.
- McPhillips J, Murphy A, Jonsson MP, Hendren WR, Atkinson R *et al*. High-performance biosensing using arrays of plasmonic nanotubes. *ACS Nano* 2010; **4**: 2210–2216.
- Shen Y, Zhou JH, Liu TR, Tao YT, Jiang RB *et al*. Plasmonic gold mushroom arrays with refractive index sensing figures of merit approaching the theoretical limit. *Nat Commun* 2013; **4**: 2381.
- Svedendahl M, Chen S, Dmitriev A, Käll M. Refractometric sensing using propagating versus localized surface plasmons: a direct comparison. *Nano Lett* 2009; **9**: 4428–4433.
- Ament I, Prasad J, Henkel A, Schmachtel S, Sönnichsen C. Single unlabeled protein detection on individual plasmonic nanoparticles. *Nano Lett* 2012; **12**: 1092–1095.
- Beuwer MA, Prins MW, Zijlstra P. Stochastic protein interactions monitored by hundreds of single-molecule plasmonic biosensors. *Nano Lett* 2015; **15**: 3507–3511.
- Dahlin AB. Size matters: problems and advantages associated with highly miniaturized sensors. *Sensors* 2012; **12**: 3018–3036.
- Šipová H, Vrba D, Homola J. Analytical value of detecting an individual molecular binding event: the case of the surface plasmon resonance biosensor. *Anal Chem* 2011; **84**: 30–33.
- Thorsen T, Maerkl SJ, Quake SR. Microfluidic large-scale integration. *Science* 2002; **298**: 580–584.
- García-Cordero JL, Maerkl SJ. A 1024-sample serum analyzer chip for cancer diagnostics. *Lab Chip* 2014; **14**: 2642–2650.
- Marie R, Dahlin AB, Tegenfeldt JO, Höök F. Generic surface modification strategy for sensing applications based on Au/SiO<sub>2</sub> nanostructures. *Biointerphases* 2007; **2**: 49–55.
- Marie R, Beech JP, Vörös J, Tegenfeldt JO, Höök F. Use of PLL-g-PEG in micro-fluidic devices for localizing selective and specific protein binding. *Langmuir* 2006; **22**: 10103–10108.
- Huang B, Wu HK, Kim S, Zare RN. Coating of poly (dimethylsiloxane) with n-dodecyl-β-D-maltoside to minimize nonspecific protein adsorption. *Lab Chip* 2005; **5**: 1005–1007.
- Viefhues M, Manchanda S, Chao T-C, Anselmetti D, Regtmeier J *et al*. Physisorbed surface coatings for poly (dimethylsiloxane) and quartz microfluidic devices. *Anal Bioanal Chem* 2011; **401**: 2113–2122.
- Boozer C, Yu QM, Chen SF, Lee C-Y, Homola J *et al*. Surface functionalization for self-referencing surface plasmon resonance (SPR) biosensors by multi-step self-assembly. *Sensors Actuat B Chem* 2003; **90**: 22–30.
- Keefe AJ, Brault ND, Jiang SY. Suppressing surface reconstruction of superhydrophobic PDMS using a superhydrophilic zwitterionic polymer. *Biomacromolecules* 2012; **13**: 1683–1687.
- Hua BY, Han KY, Zhou RB, Kim H, Shi XH *et al*. An improved surface passivation method for single-molecule studies. *Nat Methods* 2014; **11**: 1233–1236.
- Norde W. Driving forces for protein adsorption at solid surfaces. *Macromol Symp* 1996; **103**: 5–18.
- Lee JN, Park C, Whitesides GM. Solvent compatibility of poly (dimethylsiloxane)-based microfluidic devices. *Anal Chem* 2003; **75**: 6544–6554.
- Dmitriev A, Hägglund C, Chen S, Fredriksson H, Pakizeh T *et al*. Enhanced nanoplasmonic optical sensors with reduced substrate effect. *Nano Lett* 2008; **8**: 3893–3898.
- Chen PY, Chung MT, McHugh W, Nidetz R, Li YW *et al*. Multiplex serum cytokine immunoassay using nanoplasmonic biosensor microarrays. *ACS Nano* 2015; **9**: 4173–4181.
- Verellen N, Van Dorpe P, Huang CJ, Lodewijks K, Vandenbosch GAE *et al*. Plasmon line shaping using nanocrosses for high sensitivity localized surface plasmon resonance sensing. *Nano Lett* 2011; **11**: 391–397.
- Otte MA, Estévez M-C, Carrascosa LG, González-Guerrero AB, Lechuga LM *et al*. Improved biosensing capability with novel suspended nanodisks. *J Phys Chem C* 2011; **115**: 5344–5351.
- Cetin AE, Etezadi D, Altug H. Accessible nearfields by nanoantennas on nanopleds for ultrasensitive vibrational spectroscopy. *Adv Opt Mater* 2014; **2**: 866–872.
- Aćimović SS. Localized surface plasmon resonance for biosensing lab-on-a-chip applications. PhD thesis, Universitat Politècnica de Catalunya, Castelldefels, Spain, 2012.
- Aćimović SS, Ortega MA, Sanz V, Berthelot J, Garcia-Cordero JL *et al*. LSPR chip for parallel, rapid, and sensitive detection of cancer markers in serum. *Nano Lett* 2014; **14**: 2636–2641.
- Ruemmele JA, Hall WP, Ruvuna LK, Van Duyne RP. A localized surface plasmon resonance imaging instrument for multiplexed biosensing. *Anal Chem* 2013; **85**: 4560–4566.
- Yoshikawa H, Murahashi M, Saito M, Jiang S, Iga M *et al*. Parallelized label-free detection of protein interactions using a hyper-spectral imaging system. *Anal Methods* 2015; **7**: 5157–5161.
- Johnson PB, Christy R-W. Optical constants of the noble metals. *Phys Rev B* 1972; **6**: 4370–4379.
- Cheng T-L, Cheng C-M, Chen B-M, Tsao D-A, Chuang K-H *et al*. Monoclonal antibody-based quantitation of poly (ethylene glycol)-derivatized proteins, liposomes, and nanoparticles. *Bioconjugate Chem* 2005; **16**: 1225–1231.
- Hanarp P, Käll M, Sutherland DS. Optical properties of short range ordered arrays of nanometer gold disks prepared by colloidal lithography. *J Phys Chem B* 2003; **107**: 5768–5772.
- Andersson A-S, Glasmästar K, Hanarp P, Seantier B, Sutherland DS. Patterning colloidal monolayer films using microcontact particle stripping. *Nanotechnology* 2007; **18**: 205303.
- Dahlin AB, Tegenfeldt JO, Höök F. Improving the instrumental resolution of sensors based on localized surface plasmon resonance. *Anal Chem* 2006; **78**: 4416–4423.
- Junesch J, Emilsson G, Xiong KL, Kumar S, Sannomiya T *et al*. Location-specific nanoplasmonic sensing of biomolecular binding to lipid membranes with negative curvature. *Nanoscale* 2015; **7**: 15080–15085.
- Emilsson G, Schoch RL, Feuz L, Höök F, Lim RYH *et al*. Strongly stretched protein resistant poly (ethylene glycol) brushes prepared by grafting-to. *ACS Appl Mater Interfaces* 2015; **7**: 7505–7515.
- Rosano C, Arosio P, Bolognesi M. The X-ray three-dimensional structure of avidin. *Biomol Eng* 1999; **16**: 5–12.
- Lee SH, Lindquist NC, Wittenberg NJ, Jordan LR, Oh S-H. Real-time full-spectral imaging and affinity measurements from 50 microfluidic channels using nanohole surface plasmon resonance. *Lab Chip* 2012; **12**: 3882–3890.
- Im H, Shao HL, Park YI, Peterson VM, Castro CM *et al*. Label-free detection and molecular profiling of exosomes with a nano-plasmonic sensor. *Nat Biotechnol* 2014; **32**: 490–495.



This work is licensed under a Creative Commons Attribution-NonCommercial-NoDerivs 4.0 International License. The images or other third party material in this article are included in the article's Creative Commons license, unless indicated otherwise in the credit line; if the material is not included under the Creative Commons license, users will need to obtain permission from the license holder to reproduce the material. To view a copy of this license, visit <http://creativecommons.org/licenses/by-nc-nd/4.0/>

© The Author(s) 2017

Supplementary Information for this article can be found on the *Light: Science & Applications*' website (<http://www.nature.com/lisa>).